Shock Oscillation Mechanism of Highly Separated Transitional Shock-Wave/Boundary-Layer Interactions

Nel, Philipp L.; Schreyer, Anne Marie; Schrijer, Ferry F.J.; van Oudheusden, Bas W.; Janke, Christian; Vasilopoulos, Ilias; Swoboda, Marius

DOI
10.2514/1.J064567

Publication date
2025

Published in
AIAA Journal

Citation (APA)
Nel, P. L., Schreyer, A. M., Schrijer, F. F. J., van Oudheusden, B. W., Janke, C., Vasilopoulos, I., & Swoboda, M. (2025). Shock Oscillation Mechanism of Highly Separated Transitional Shock-Wave/Boundary-Layer Interactions. *AIAA Journal*, *63*(5), 1703-1715. https://doi.org/10.2514/1.J064567

AIAA JOURNAL
Vol. 63, No. 5, May 2025

Shock Oscillation Mechanism of Highly Separated Transitional Shock-Wave/Boundary-Layer Interactions

Philipp L. Nel* and Anne-Marie Schreyer†
RWTH Aachen University, 52062 Aachen, Germany
Ferry F. J. Schrijer‡ and Bas W. van Oudheusden§
Delft University of Technology, 2629 HS Delft, the Netherlands
and
Christian Janke,¶ Ilias Vasilopoulos,** and Marius Swoboda††
Rolls-Royce Germany Ltd. & Co. KG, Brandenburg 15827, Germany

https://doi.org/10.2514/1.J064567

Reynolds numbers at cruise altitude can be such that a laminar boundary layer persists on the suction side of a transonic fan blade up to the shock-wave/boundary-layer interaction (SBLI). In a transitional SBLI which exhibits sufficiently large shock-induced separation, a shock oscillation mechanism characterized by growth and natural suppression of the upstream laminar section of the separation bubble occurs. To validate the shock oscillation mechanism observed in large eddy simulations (LES), the shock oscillation mechanism is studied experimentally using high-speed Schlieren and spark-light shadowgraphy. A characteristic length based on the distance of laminar separation shock travel is proposed. Strouhal numbers from LES and the experiment collapse at around 0.075. A strong dependency of the oscillation mechanism on free-stream turbulence and boundary-layer state is shown. Dominant oscillation frequencies are an order of magnitude lower for the turbulent interaction as opposed to the laminar case. For the laminar case, dynamic mode decomposition showed a strong relationship of the laminar separation shock with the separation bubble and reflected shock movement. The turbulent interaction shows a significantly lower reflected shock travel distance. The findings experimentally confirm that stabilization of the shock is achieved by tripping the boundary layer.

Nomenclature

Ma	=	Mach number
P_t	=	total pressure
Re	=	Reynolds number
St	=	Strouhal number
TI	=	turbulence intensity
T_t	=	total temperature
Δt	=	time step
Δx^+	=	nondimensional grid spacing in streamwise direction
Δy^+	=	nondimensional grid spacing in wall normal direction
Δz^+	=	nondimensional grid spacing in spanwise direction
δ	=	boundary-layer thickness
δ^*	=	displacement thickness
σ_n	=	normalized standard deviation
θ	=	momentum thickness
θ_{SG}	=	shock generator deflection angle

I. Introduction

FOR transonic fans in aircraft engines of smaller size (business jet and defense applications) at cruise altitude, strong shock-induced separation and shock-wave/boundary-layer interactions (SBLIs) exist, causing shock oscillations which excite fan blade structural modes if not mitigated. The present work focuses on investigating the shock oscillation mechanism present in highly separated (strong) oblique SBLIs, because these interactions exhibit the same oscillation mechanism as on the altitude fan case [1]. In Nel et al. [1] it was seen that the shock oscillation in transonic fans appears to be a function of the conditions at the SBLI itself (laminar boundary-layer state, separation severity, upstream shear layer transition), rather than being dependent on the compressor-like geometry. This observation is supported by findings from studies on SBLIs on compression ramps and impinging shock waves, where low-frequency oscillations are linked to the interaction dynamics [2,3]. Furthermore, in experimental cascade studies, Nel et al. [4] concluded that compressor cascades were unsuitable for showing the expected mechanism of shock oscillation, likely due to other sources of shock oscillation which dominate the flow field and failing to represent the oscillation mechanism occurring on transonic fans at cruise altitude. It was clear that a cleaner, canonical experiment was needed for validating the mechanism seen in large eddy simulations (LES) with quiet inflow conditions. Therefore, Nel et al. [1] sought to find a research configuration using LES, where the same shock oscillation mechanism could be shown. The study concluded that the problem of shock oscillation on a highly loaded transonic fan at altitude could be simplified (Fig. 1) to a highly separated laminar oblique SBLI with transition on the shear layer of the upstream laminar separation.

To achieve a better understanding of the dynamic mechanisms, the canonical research configuration is realized in a supersonic wind tunnel and studied experimentally in the current work, after which the oscillation mechanism observed in LES simulations can be validated and used to support the experimental results.

Nel et al. [1] describe the features defining the shock oscillation mechanism of interest as follows:

The shock oscillation features a periodically collapsing separation bubble with Kelvin–Helmholtz instabilities on the shear layer upstream of the shock. This separation bubble grows in the upstream direction, pulling the instabilities with it in front of the shock wave. At a far enough upstream position, the turbulence from these instabilities is significant enough to wash away (or suppress) a significant part of the separation bubble, especially the upstream laminar

Received 10 July 2024; revision received 22 October 2024; accepted for publication 4 November 2024; published online 29 November 2024.

*Ph. D. Candidate, Institute of Jet Propulsion and Turbomachinery, Templergraben 55; Nel@IST.RWTH-Aachen.de (Corresponding Author).
†Head of Research Group, Institute of Aerodynamics, Wüllnerstraße 5a.
‡Assistant Professor, Flow Physics and Technology, Department of Aerodynamics, Faculty of Aerospace Engineering, Kluyverweg 1.
§Associate Professor, Flow Physics and Technology, Department of Aerodynamics, Faculty of Aerospace Engineering, Kluyverweg 1.
¶Development Engineer, Fans and Compressors, Blankenfelde-Mahlow.
**CFD Methods Developer, Turbines, Blankenfelde-Mahlow.
††Honorary Professor, Head of Science and Capability, Blankenfelde-Mahlow.

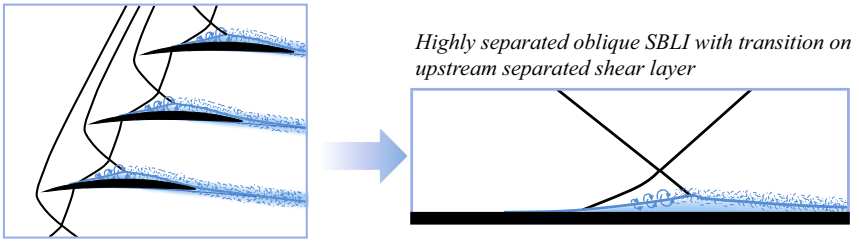

Fig. 1 Simplified case as according to the conclusions of Nel et al. [1]. Adapted with permission.

section, at which stage the turbulence is no longer generated upstream of the shock and the separation bubble can start to grow again. The upstream growth is highlighted by the formation of a separation shock. If the boundary layer exhibits significant upstream disturbances, such as in the presence of a tripping device, the oscillation amplitude is significantly reduced compared to the laminar case.

Indeed, one can see from literature that most studies on shock oscillations from oblique SBLIs are focused on turbulent incoming boundary layers, as this configuration most often occurs in practice [5–7]. More specifically, the focus has been on understanding the low-frequency unsteadiness observed in shock-wave/turbulent-boundary-layer interactions, particularly when the shock strength is sufficient to induce separation in the boundary layer. This separation leads to low-frequency unsteadiness in the separation bubble and the separation shock, with characteristic frequencies significantly lower than those of the incoming boundary layer [8]. The unsteadiness in shock-induced separation has been confirmed in various types of SBLIs, such as compression ramps or impinging shock waves, where low-frequency movements of the separated region and upstream shock-wave motions have been observed [2]. The turbulence of the incoming boundary layer has been identified as a significant factor responsible for the motion of shock waves in these interactions [3]. Studies have also explored the role of oblique shock waves impinging on laminar boundary layers, highlighting the unsteady characteristics of these interactions [9]. However, these studies are often cases where transition occurs downstream of the impingement, with relatively low flow deflection angles [10]. The unsteadiness of shock waves has been found to increase with shock intensity, and SBLIs can exhibit unsteadiness regardless of the laminar or turbulent nature of the incoming boundary layer [11].

Experimental studies have shown that the unsteadiness in SBLIs is associated with large-scale structures in the boundary layer. For instance, Beresh et al. (2002) and Ganapathisubramani et al. (2007) observed that upstream turbulent boundary-layer fluctuations are correlated with the motion of the separation shock [5,12]. These studies highlight the presence of large streamwise vortices, which are similar to the superstructures observed in subsonic turbulent boundary layers, as potential sources of low-frequency unsteadiness in turbulent SBLIs.

Numerical simulations have provided complementary insights into the unsteady behavior of SBLIs. Studies by Wu and Martin (2008) and Touber and Sandham (2008) using direct numerical simulation (DNS) have shown the presence of coherent structures and their influence on shock motion [6,13]. These simulations indicate that the dynamics of the separated bubble are closely linked to the shock movements, although there is still some debate regarding the primary source of the unsteadiness.

Babinsky and Harvey (2011) found that the unsteady behavior of SBLIs can be broadly classified based on the interaction type and flow conditions: separated flows with far-downstream influence exhibit unsteadiness driven by downstream instabilities, where the size and behavior of the separation bubble are significantly influenced by the downstream flow conditions [14]. In contrast, separated flows without far-downstream influence are primarily driven by upstream disturbances, such as large-scale vortices in the incoming boundary layer [14]. For unseparated flows, the shock-induced boundary-layer interaction exhibits less pronounced unsteadiness, and the shock oscillations are typically of higher frequency compared to separated flows [7].

Effective control of SBLI unsteadiness is critical for improving the performance and stability in high-speed applications. Control strategies can be classified into passive and active methods. Passive control techniques such as surface roughness, vortex generators, and passive cavity structures have been employed to manipulate the boundary layer and mitigate unsteady effects [14]. Active control methods involving actuators and synthetic jets have shown promise in actively controlling the boundary-layer characteristics and reducing unsteady shock motions [7].

In the current paper, we shall focus on a highly separated transitional oblique SBLI, where transition of the laminar boundary layer occurs just upstream of the impingement on the separated (originally laminar) shear layer. The experiment should firstly show the low-frequency unsteadiness of the reflected shock (linked to the unsteadiness of the separation bubble and therefore separation shock at the same frequency) and, secondly, that the transition location is upstream of the shock wave on the shear layer of the laminar separation bubble and that this transition location is also shifting periodically [1]. If this can be shown, with a clear qualitative match in the behavior of the experimentally observed oscillation mechanisms to that of the numerical simulations, the numerical approach to resolving the shock oscillation mechanism of the case simplification proposed in Nel et al. [1] is verified and validated by experimentally showing matching physical mechanisms of shock oscillation of the proposed SBLI configuration, which has a matching shock oscillation mechanism to the transonic fan LES case.

II. Experimental Setup

Because of the successful use of spark-light Schlieren imaging to visualize transition by Giepman [10] and the variable throat allowing an adjustable Mach number, the TST-27 blowdown wind tunnel at the Technical University of Delft (TU Delft) is employed for our experiments (Fig. 2).

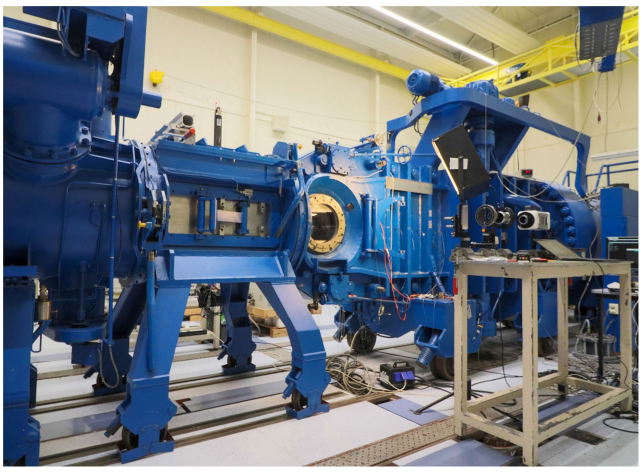

Fig. 2 TST-27 facility at TU Delft.

The wind tunnel was operated in a supersonic configuration (opened transonic throat), as shown in Fig. 3, where the Mach number can be adjusted with a continuously adjustable throat (Ma 1.15–4.2).

The TST-27 blowdown transonic/supersonic wind tunnel features a 28 cm by 28 cm test section cross section. Air is supplied from a 300 m^3 storage vessel charged to 42 bar and stored at ambient temperature, allowing blowdown operation of the tunnel for approximately 300 s, with typical run times restricted to less than 30 s to maintain stable conditions. During these runs, the total temperature in the test section decreases slightly by approximately 4–5 K. The test section offers optical access through large windows on both sides, facilitating flow visualization techniques such as Schlieren photography and particle image velocimetry (PIV) [10]. The settling chamber of the wind tunnel has a square cross section of 800 mm × 800 mm, and the converging nozzle contracts laterally to a final constant channel width of 280 mm. The nozzle's upper and lower walls provide a continuously adjustable contoured converging–diverging shape to produce the required Mach number in the test section. The distance from the throat to the center of the test section is approximately 2 m [10].

Preparatory LES simulations [1] indicated that the oscillation mechanism becomes prominent only under certain highly separated conditions. However, not all of the numerically studied conditions can be replicated in practical experiments, as large deflection angles often result in excessive blockage. Therefore, initial experimental tests focused on identifying a practical condition and geometry for which the shock oscillation mechanism could be clearly observed. A range of test conditions explored during this phase is presented in the Appendix. Furthermore, the shock impingement location should be close to the leading edge, without the upstream part of the unsteady laminar separation spilling over the leading edge. The conditions which were finally chosen are $\theta_{SG} = 19$ deg (shock generator deflection angle), Ma = 2.3, and $P_t = 2.8$ bar. The total temperature is assumed to be 293 K.

The test section model is shown in Fig. 4. A sketch of the model assembly is provided in Fig. 5. A laminar case, as well as a tripped boundary-layer case (Fig. 6), are studied. For the tripped case, a 100 μm × 1.3 mm strip of double-sided tape with silicon carbine particles applied to the top surface is applied 3 mm from the leading edge. The step height is based on previous studies [4,15]. The

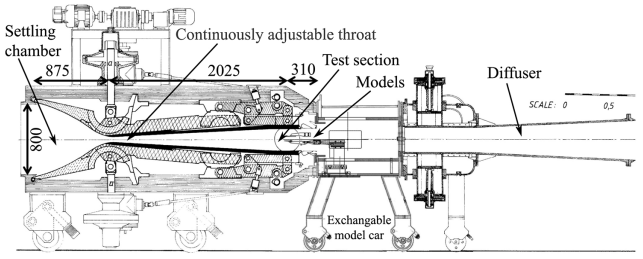

Fig. 3 TST-27 in supersonic configuration (adapted with permission from Giepman [10]).

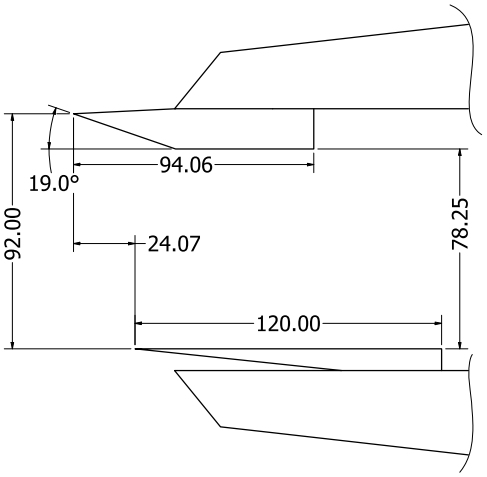

Fig. 5 Wind tunnel model assembly sketch. The span-wise dimension of flat plate and shock generator is 276 mm.

resulting shock wave impinges at 60 mm from the leading edge of a flat plate, with the laminar part of the separation extending upstream to as far as 10 mm from the leading edge. The free-stream unit Reynolds number is 5.48E4 [mm^{-1}]. The free-stream turbulence level (at Mach 1.7) has been reported to be $u' = 0.6\%$ and $v' = 0.4\%$ [10]. Without the impinging shock, the laminar boundary layer on the flat plate would have a theoretical [16] thickness of $\delta = 0.162$ mm, a displacement thickness $\delta^* = 0.057$ mm, and momentum thickness of $\theta = 0.022$ mm at 60 mm from the leading edge.

We use high-speed Schlieren imaging (Photron FASTCAM NOVA S12, 100 kHz, 384 × 240 pixels, exposure time 1/300,000 s) to capture the unsteadiness of the separation bubble (and hence reflected shock), as well as the periodically visible separation shock. The Z-type Schlieren setup can be seen in Fig. 7, with a diagram of the setup found in the Appendix (Fig. 35). The high frame rate allows a detailed analysis of the dynamic mechanisms, such as the upstream propagation speed of the upstream laminar separation shock, which is expected to be in the order of the upstream acoustic wave propagation velocity [1]. Furthermore, the high-speed Schlieren is used to show the difference between the frequency of dominant oscillation modes of the laminar vs the tripped (turbulent boundary-layer) case. In addition, spark-light shadowgraphy (20 ns light bursts) is used to capture the transition location with a higher resolution camera (Lavision Imager LX, 1624 × 1236 pixels). A surface oil-flow visualization is used to gauge the 3D nature of the separation bubble. A mixture of Shell Tellus type 22 oil and titanium dioxide TiO_2 particles (Sachtleben UV-TITAN L-530, 30 nm crystal size) was applied to the surface of the flat plate with a brush. A Canon EOS 250D DSLR camera (6000 × 4000 pixels) was used with a 135 mm telephoto lens, allowing a perspective transform in postprocessing. A circular polarization filter was used to minimise reflections. The test section was illuminated with LED lights.

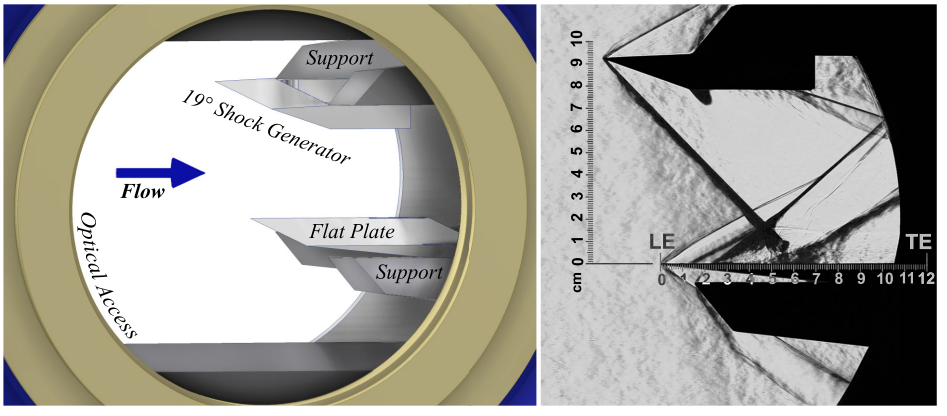

Fig. 4 Left: model in experimental setup of TU Delft TST-27 Transonic/Supersonic wind tunnel. Right: Schlieren photograph with vertical knife edge.

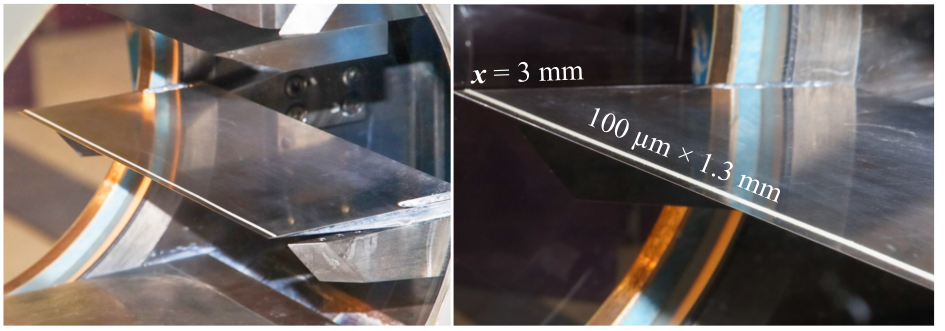

Fig. 6 a) Flat plate overview with transition strip. b) Transition strip specifications.

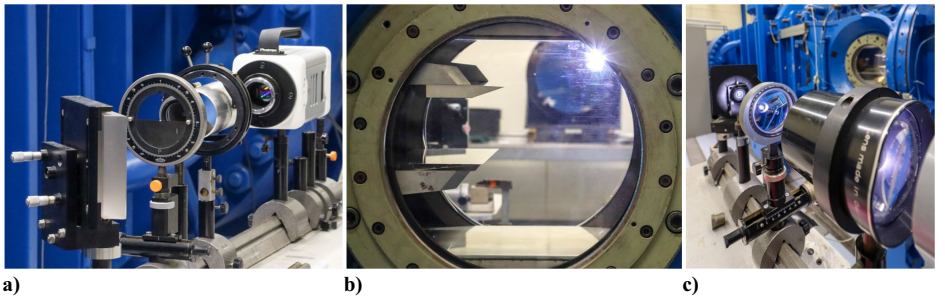

Fig. 7 a) Knife edge and lens setup with high-speed camera. b) View of parabolic mirror through test section. c) Light source focusing.

III. Surface Oil-Flow Visualization

To achieve an overview of the flow topology, we carried out surface oil-flow visualizations. The oil-flow visualization photograph was taken during the wind tunnel run to avoid oil spillage. From the surface oil-flow visualization in Fig. 8, a fairly symmetrical interaction can be observed. However, as is often unavoidable in wind tunnel tests, the overall interaction exhibits a 3D nature with significant corner effects. This should be kept in mind when comparing the experimental results with the simulations.

IV. High-Speed Schlieren/Shadowgraphy

A range of Schlieren knife edge settings was tested and used to analyze different aspects of the flow field. The laminar separation shock is especially clear when using a vertical knife edge (Fig. 9) to bend light in the horizontal plane, thereby emphasizing the horizontal gradient component and avoiding oversaturation of the separation or near-wall shear effects. Note that in the case of the shadowgraph (Fig. 10), the laminar separation shock is barely visible, due to the fact that it is relatively weak. Therefore, we choose the Schlieren configuration with vertical knife edge for the analysis. A series of instantaneous snapshots for one oscillation cycle is shown in Fig. 11. Using particle image velocimetry from a related study by the authors [17], which highlights the relationship between the separation

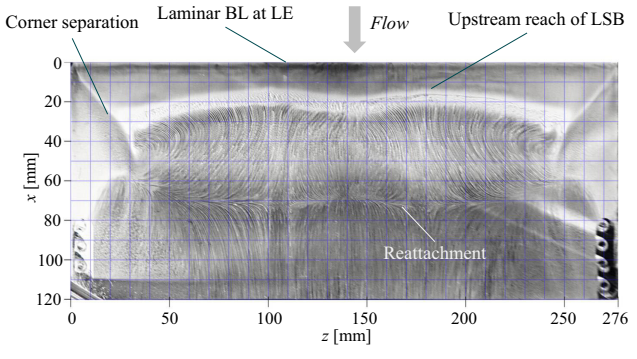

Fig. 8 Surface oil-flow visualization at Ma 2.3 and 2.8 Bar.

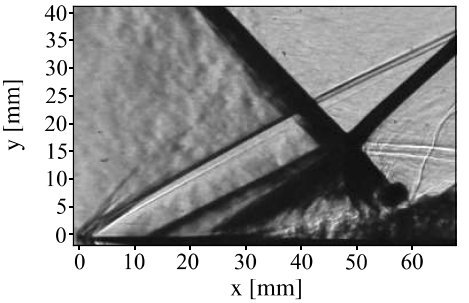

Fig. 9 Laminar case: instantaneous high-speed Schlieren capturing upstream growth phase of laminar section of separation.

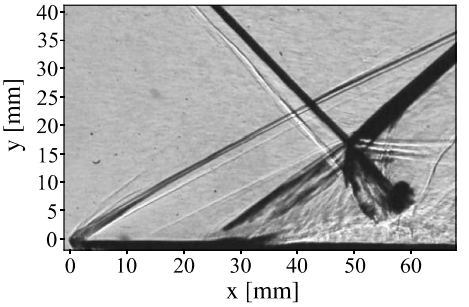

Fig. 10 Laminar case: instantaneous high-speed shadowgraph corresponding to the same phase of the oscillation as Fig. 9.

bubble, Mach stem, and the forward and backward states of shock oscillation, the flow features at the mid-plane during the grown upstream phase of the laminar section of the separation bubble are illustrated in Fig. 12. The periodic appearance and upstream propagation of the laminar separation shock affects the separation bubble through entrainment of generated instabilities into the separation bubble, which affects the reflected shock wave. The frequency of this occurrence, which dominates the flow field, is analyzed with dynamic mode decomposition (DMD) in Sec. IV.A. The forward and backward states of the shock oscillation with laminar oncoming

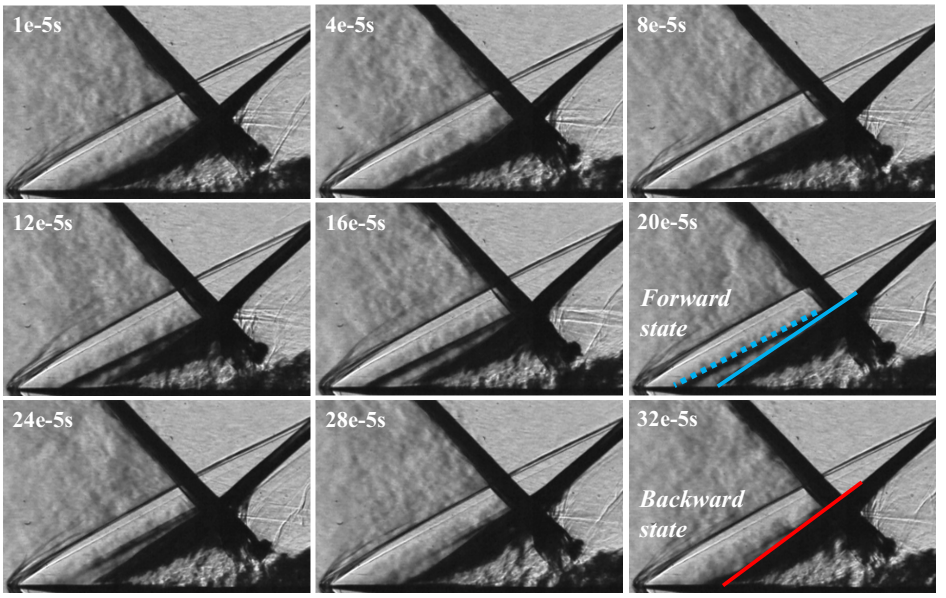

Fig. 11 Laminar case: instantaneous high-speed Schlieren snapshots showing oscillation cycle.

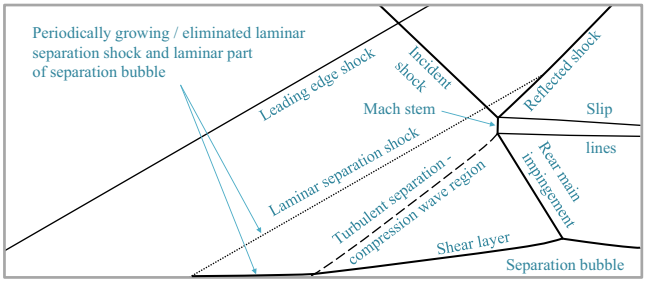

Fig. 12 Flow structure at mid-plane with laminar oncoming boundary layer, showing oscillation state where laminar section of separation bubble grows in the upstream direction.

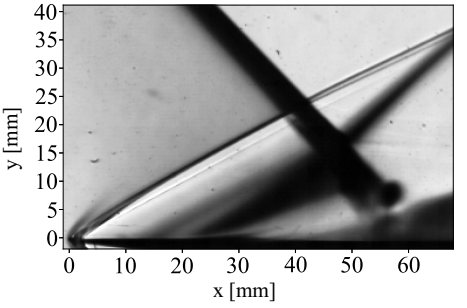

Fig. 14 Laminar case: time averaged high-speed Schlieren with vertical knife edge.

boundary layer are shown in Fig. 13. The Mach stem feature cannot clearly be seen in Schlieren images due to the side wall effects.

Aside from showing the oscillation mode associated with the laminar SBLI, another objective of the high-speed Schlieren imaging is a comparison between the laminar and tripped (turbulent boundary-layer) cases. The tripped case is captured using the same settings as the laminar case, and the results compared. Figures 14 and 15 show the time-averaged Schlieren sequences of the laminar and tripped cases, respectively. The corresponding standard deviations of these Schlieren sequences are shown in Figs. 16 and 17. When comparing the laminar case to the tripped case, the tripped time-averaged Schlieren (Fig. 15) already reveals the relatively stable shear layer originating from the turbulent separation bubble, which detaches at approximately $x = 27$ mm. Having a look at the standard deviation, the laminar case exhibits significant movement

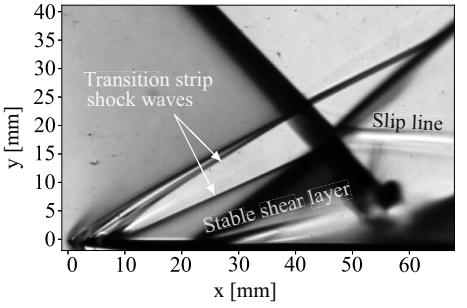

Fig. 15 Tripped case: time averaged high-speed Schlieren with vertical knife edge.

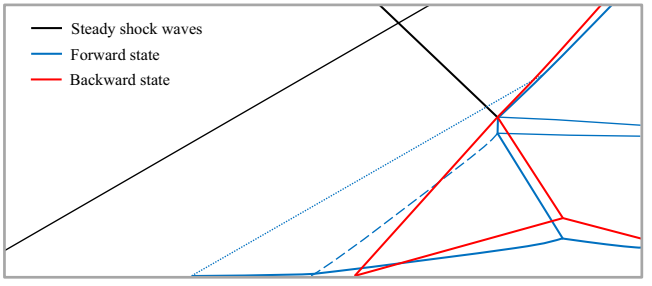

Fig. 13 Flow structure at mid-plane with laminar oncoming boundary layer, showing oscillation forward and backward states.

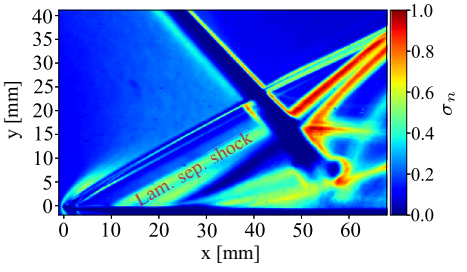

Fig. 16 Laminar case: normalized standard deviation of high-speed Schlieren with vertical knife edge.

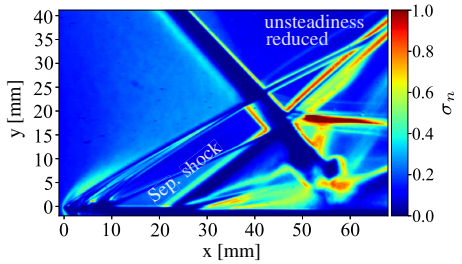

Fig. 17 Tripped case: normalized standard deviation of high-speed Schlieren with vertical knife edge.

in the laminar separation shock region (emanating between $x = 10$ and 22 mm). Conversely, the tripped case exhibits a relatively insignificant deviation of the separation shock (emanating between $x = 20$ and 22 mm). For the tripped case, the standard deviation is nondimensionalised with the maximum value of the laminar case in order to compare the cases. Furthermore, one can clearly see from the standard deviation a reduced reflected shock travel distance for the tripped case compared to the laminar case. Another notable difference is that the reflected shock is positioned slightly upstream in the tripped case. Furthermore, a slip line is clearly visible for the tripped time averaged case, because of the fact that it is relatively stable. The slip line emanates from a Mach stem, which is not clearly visible here due to the spanwise integration of the Schlieren setup. However, the Mach stem is visible in the instantaneous high-speed shadowgraphs (Fig. 10) or spark-light shadowgraphs (Fig. 26) and CFD calculations (Fig. 30c) later on. Overall, the averaged and standard deviation results show the stabilizing effect of tripping the boundary layer on the separation shock and reflected shock travel distance.

A. Unsteady Analysis

In this section, the unsteady behavior captured by the high-speed Schlieren is analyzed to get access to the dynamic mechanisms of the flow field. To evaluate the upstream propagation velocity of the laminar separation bubble, the separation shock position with time is plotted in Fig. 18. The laminar separation shock position is tracked based on the point of maximum gradient of the high-speed Schlieren with a vertical knife edge at the point of emanation on the flat plate. The dashed blue lines indicate a propagation velocity of 66 m/s.

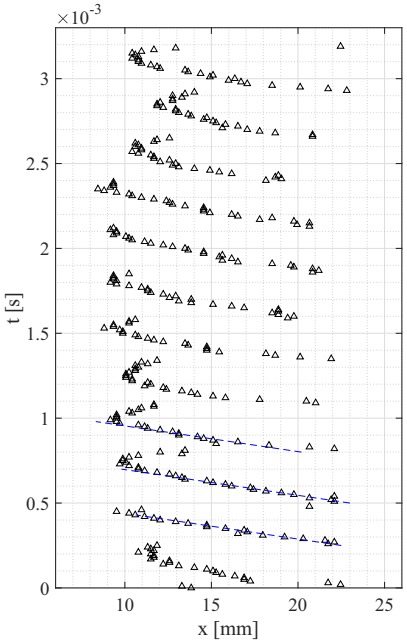

Fig. 18 Separation shock position extracted from high-speed Schlieren. Dashed blue lines indicate a propagation velocity of 66 m/s.

Note that the laminar separation shock travel distance is around 11.5 mm on average, which is a characteristic length-scale for the shock oscillation mechanism. The behavior of the separation shock position with time qualitatively agrees with our previous findings based on the isentropic Mach number distribution from DNS in Nel et al. [1], which also shows the periodic pattern of the upstream laminar separation shock, with a dominant forward movement before vanishing back to the point of turbulent separation. At the same time of vanishing, another laminar speration shock forms and starts to grow upstream. The reason the forward movement shows a pronounced separation shock is because the shape of the laminar upstream part detaches from the surface in a steeper shape for the upstream growth phase of the separation bubble, whereas it collapses in a concave fashion. This has been shown in previous studies [1] and can also be seen in the LES simulations later on: Fig. 30a corresponds to the upstream growth phase and a steep separation exists, whereas Fig. 30b corresponds to the start of the collapse phase, where the separation bubble geometry becomes almost tangential to the flat plate at the point of emanation. For convenience, the figure is reproduced in the Appendix (Fig. 36).

The spatially and temporally coherent modes of the shock unsteadiness are evaluated using sparsity promoting optimized DMD [18,19]. In this variant of the standard DMD [20], backpropagation and stochastic gradient descent techniques from machine learning are employed to optimize the eigenvalues and eigenvectors for the DMD operator. This has the advantage of being more robust to noise and promoting sparsity to help identify the most significant dynamics and filter out less important or spurious modes. The batch size, which is the number of samples used in one forward and backward pass through the parameters being optimized, is kept at the standard recommended value of $N_{\text{batch}} = 32$. For each case, the optimal rank truncation is chosen by the singular value hard thresholding algorithm [21]. The relative importance I_{rel} refers to the contribution of each DMD mode to the overall dynamics.

The DMD spectra of dominant modes resulting from the analysis on the laminar case are shown in Figs. 19a and 19b. Observe that for the laminar case, one dominant mode is identified at 3748 Hz which describes 62% of the dynamic behavior of the Schlieren sequence. The associated mode shape of the Schlieren sequence is shown in Fig. 21. The quantity shown is the Schlieren intensity captured by the mode, scaled by the relative intensity I_{rel} of the mode. This mode is associated with the periodic appearance of the separation shock, which can be explained by a periodic upstream growth of the laminar part of the separation bubble. As the separation bubble grows in the upstream direction, the laminar part brings with it instabilities on the separated shear layer in the upstream direction. This laminar part is by nature extremely thin, and therefore when it reaches a certain length (the characteristic length scale of the oscillation frequency), the turbulence originating from Kelvin–Helmholtz instabilities on the laminar shear layer suppress the upstream laminar part of the separation bubble by entrainment, effectively cutting off the laminar part, leading to its collapse. As the instabilities from the vanishing upstream part advect over the separation bubble, the bulk of the separation bubble is also suppressed, leading to a significant movement of the reflected shock wave. The significant effect on the reflected shock wave, as well as on the separation bubble, can be seen from the mode shape in that there is a high correlation of the laminar separation shock with the separation bubble and reflected shock. Furthermore, the mode shape suggests that unsteadiness from the impinging shock wave does not affect this mode of shock oscillation, because the impinging shock wave is not visible through the dominant mode shape.

For the tripped case, the spectra are shown in Figs. 20a and 20b. Note that in the tripped case, the oscillatory behavior appears to be less well-defined, with multiple significant modes identified. In the tripped case, the frequency of the dominant mode is an order of magnitude smaller than in the laminar case, at 293 Hz. The associated mode shape (Fig. 22) shows that this mode is also associated with a movement of the reflected shock and turbulent separation shock, exhibiting a relatively small shock travel distance, as was already seen from the comparison of the standard deviation.

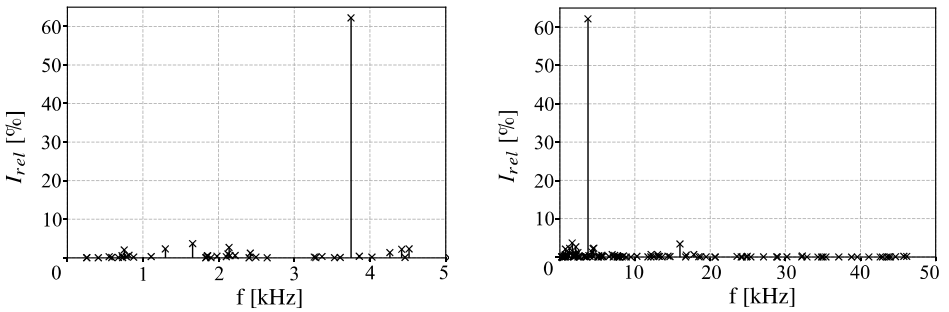

a) 5 kHz range **b) 50 kHz range**

Fig. 19 DMD spectra: laminar case.

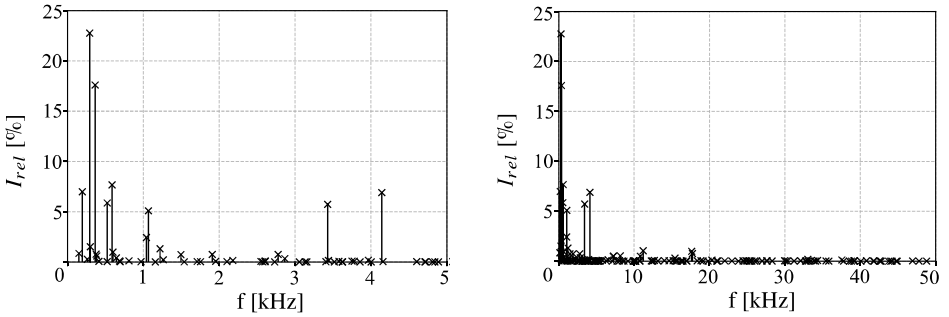

a) 5 kHz range **b) 50 kHz range**

Fig. 20 DMD spectra: tripped case.

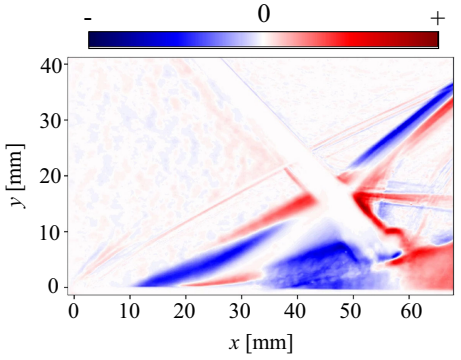

Fig. 21 Laminar case: dominant DMD mode shape ($I_{rel} = 62\%$) at 3748 Hz.

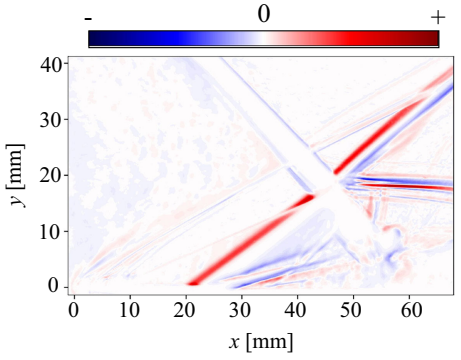

Fig. 22 Tripped case: dominant DMD mode shape cyclic temporal evolution ($I_{rel} = 23\%$) at 293 Hz.

Note that there is a behavioral difference between the laminar and the tripped dominant mode: for the laminar case, the cyclic colormap showing the mode shape is repeating from the separation shock upstream foot to the reflected shock. This means that the movement has a delay (or phase difference) in the x direction and y direction. Figure 23 shows the cyclic temporal evolution of the dominant mode in the laminar boundary-layer case. Conversely for the tripped case, the shock movement has the same phase from the point of emanation to the end of the separation shock (red across the reflected shock in the direction of the reflected shock in Fig. 22), indicating that the separation shock and reflected shock are stiff compared to the laminar case. This can also be seen in the temporal evolution of the mode for the tripped case (Fig. 24). This behavioral difference can be explained with the fact that for the laminar case, the reflected shock in this mode has an equally strong relationship with the separation bubble, which affects the flow direction in a delayed fashion because of downstream-advecting entrainment eddies from the periodic upstream instabilities, which are oscillating in their x distance from the separation bubble, and therefore in their entrainment strength. This argument is supported by the fact that the dominant mode for the tripped case shows an insignificant relationship with its separation bubble region, and hence the mechanism needed for a delayed or rolling-behavior in the reflected shock-wave movement is not present.

The spectra (Fig. 19b) show that the laminar case has a high frequency mode around 160 kHz. Although the mode also seems to be associated with turbulent structures in general, the shedding in the separation bubble is of a larger scale (Fig. 25a) and of a more coherent nature for the laminar interaction than for the turbulent one, which is split in two modes (Figs. 25b and 25c) in this region: one at 176 kHz and one at 112 kHz. It is to be expected that the laminar case shows a more structured shedding behavior in this region, due to more coherent Kelvin–Helmholtz instabilities on the laminar separated shear layer. This is perhaps also the reason that the laminar case has a single shedding mode with a relative importance of around 3%, whereas the turbulent case has several modes around this frequency, with the two dominant modes split into an importance of around 1% each.

B. Spark-Light Shadowgraphy

The purpose of this section is to provide insights into flow instabilities and transition. The shifting transition location in the laminar case was observed in the LES calculations [1]. To capture the transition location and different phases of the oscillation mechanism in more detail, the observed flow field is captured instantaneously by 20 ns light bursts. The images are background-subtracted. The full

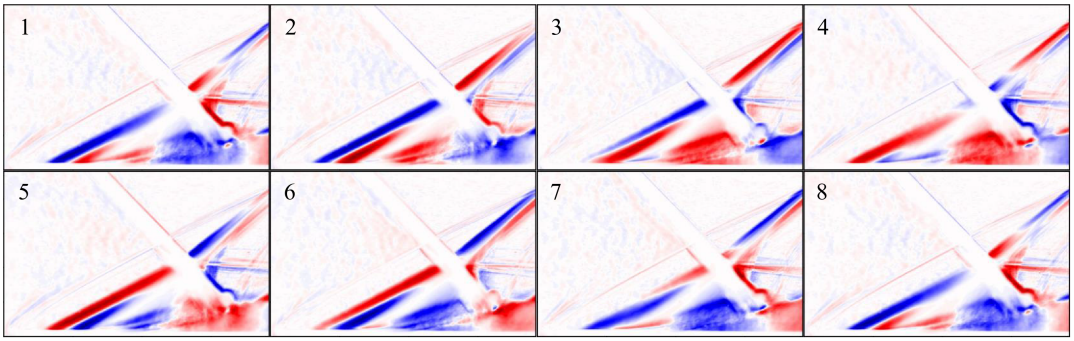

Fig. 23 Laminar case: dominant DMD mode temporal evolution ($I_{rel} = 62\%$) at 3748 Hz.

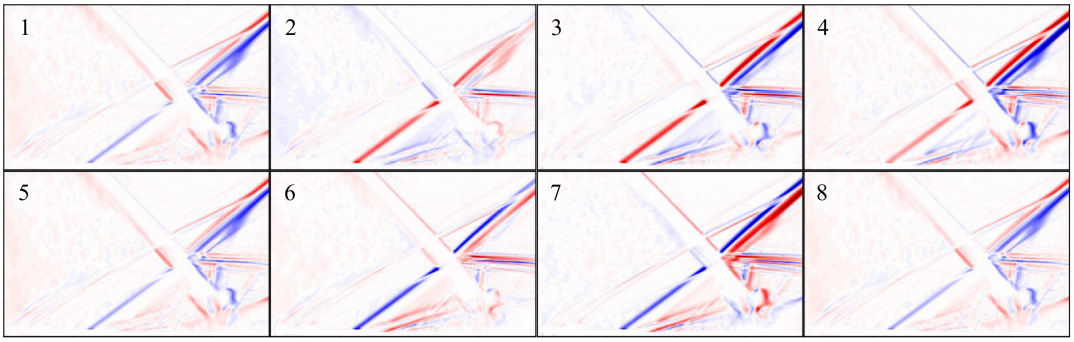

Fig. 24 Tripped case: dominant DMD mode cyclic temporal evolution ($I_{rel} = 23\%$) at 293 Hz.

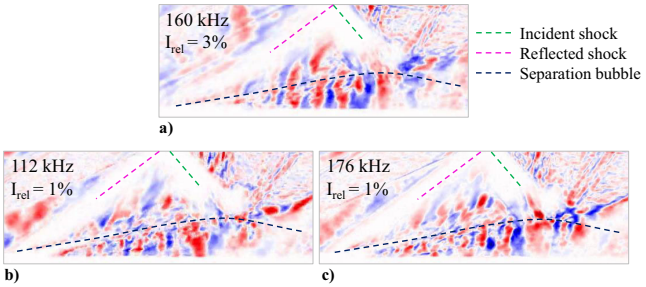

Fig. 25 Separation bubble turbulence/shedding modes: a) laminar case, single mode showing coherent structures. b) and c) Turbulent case split into two less coherent modes.

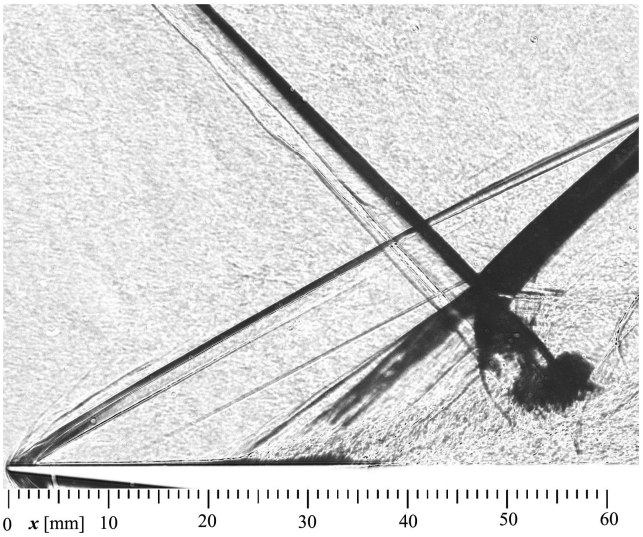

Fig. 26 Spark-light shadowgraph: overview of interaction.

frame view showing an overview of the shock interaction using this method can be seen in Fig. 26.

In Fig. 27a, we zoom in on the upstream part of the separation bubble, where one can see the separation shock from the laminar interaction, as well as the much stronger compression wave region emanating from the sudden turbulent thickening of the separation bubble (referred to as turbulent separation shock in Fig. 27a). Depending on the phase of the oscillation, this region varies between having the characteristic of densely spaced compression waves, and a single shock wave, as will be seen later on in Figs. 27b and 27a. The region where transition occurs on the shear layer can also clearly be seen in the fact that the relatively featureless laminar shear layer breaks down into turbulent structures, immediately followed by the aforementioned shock wave.

Figure 27b shows an instant where the laminar part (blue) of the separation has started to collapse; note that it is flatter than in Fig. 27a. At this stage, the separation shock from this laminar region starts to vanish due to the turbulence generated on the shear layer which suppresses the separation bubble and cuts off the upstream part of the separation bubble. For a brief moment hereafter, the interaction acts as a turbulent one, until after the upstream turbulent structures have advected downstream of the original laminar part of the separation bubble. Figure 27c shows this phase, when the originally laminar part of the separation bubble has completely vanished. The turbulent part of the separation is shown in red. Note that between the aforementioned two shadowgraphs, the transition location has shifted from 24 to 30 mm. In Fig. 27b, representing the phase where the upstream part of the separation bubble begins to vanish, the flatter nature of the upstream part of the separation bubble means that the turbulent separation shock region rather appears as multiple shock waves, or a compression wave region.

V. Numerical Investigation

During the analysis of the experimental results, the expected features based on the LES tests of Nel et al. [1] before the experiment, which were discussed in the introduction, were observed. In the current section, we perform an LES simulation based on the final experimental setup. The numerical simulations are performed with

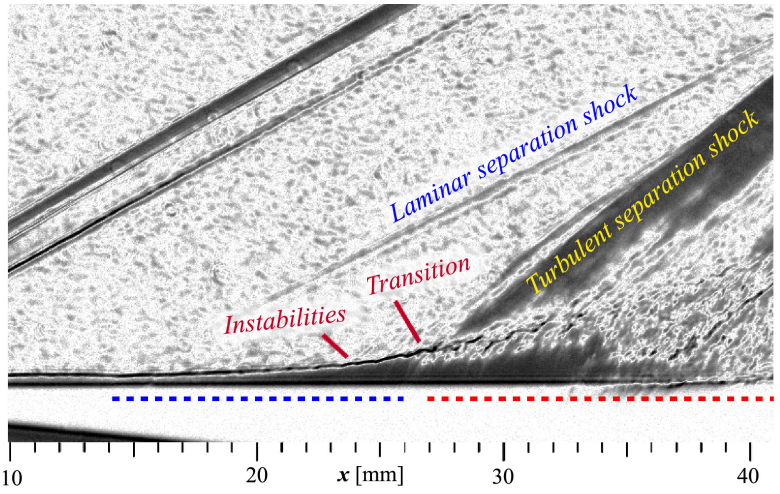

a) Growth phase of laminar part (blue). Laminar separation shock at x = 14mm, transition at x = 27mm

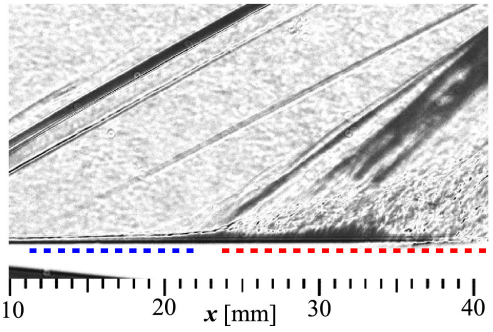

b) Collapse of laminar part (blue). Laminar separation shock at x = 11mm vanishing. Turbulence (red) at x = 24mm

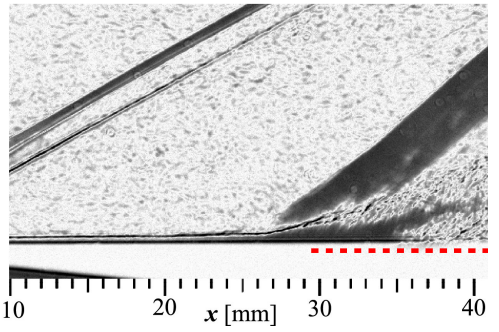

c) Collapsed laminar part of separation bubble. No visible laminar separation shock. Turbulence (red) at x = 30mm

Fig. 27 Highly separated transitional SBLI at different stages: a) growth phase, b) initial collapse, and c) complete collapse.

the Rolls-Royce *HYDRA* code, which uses second order accurate spatial and implicit dual time stepping schemes. The numerical setup has some limitations, such as not accounting for end wall separation and assuming a turbulent length scale influenced by the mesh size constraints. However, the LES simulation therefore also considers a sensitivity study to the turbulence levels.

The quasi-2D domain has a span-wise dimension (14 mm) which extends to 40% of the maximum length of the upstream influence of the SBLI during the oscillation. In Nel et al. [22], it was seen that this oscillation mechanism (in the context of a transonic fan) is independent of the extent of the span-wise direction for a span-wise dimension equaling 20% of the chord. The domain width of the current study equates to more than 20% chord-in-span, scaled relative to the upstream interaction length. The LES domain can be seen in Fig. 28. A shock generator with inviscid walls is used to generate the boundary conditions for the LES domain, which includes imposing the shock wave and an expansion fan resulting from the experimental shock generator shape. Inviscid walls are used for the lower and upper sections upstream of the flat plate and shock generator, as well as for the side walls. The pressure outlet boundary condition for the outflow should be set low enough to swallow the shock wave and sustain a supersonic flow. The maximum Courant–Friedrichs–Lewy condition is approximately 1. The Δx^+ and Δz^+ values are around 25 in the interaction region, with Δy^+ equaling 1 at the wall, and extending to a maximum of 25 in the free stream. The resulting grid has 220M cells. The grid resolution is based on the sensitivity study of Nel et al. [1], which confirms that the used grid resolution is able to resolve the oscillation mechanism.

The SIGMA subgrid scale model [23] is used to account for the unresolved turbulence scales in the simulation. A supersonic inlet

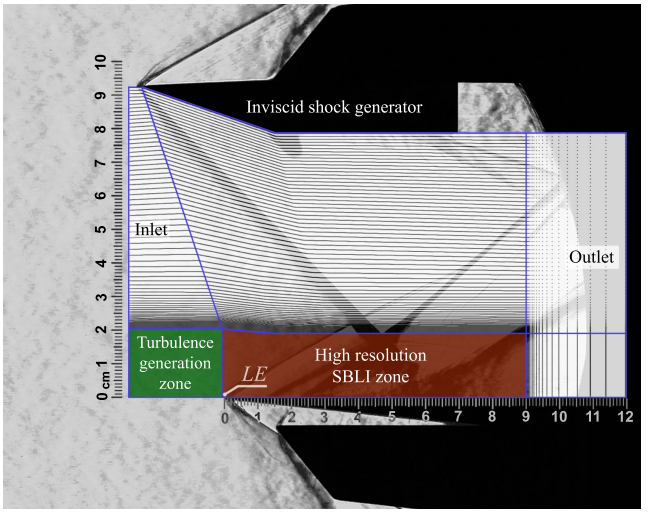

Fig. 28 Final simulation domain for experimental comparison.

boundary condition with synthetic inlet turbulence generation is employed for this simulation in order to be able to investigate the effect of turbulence. The turbulence velocity field generation follows the method of Davidson [24] which is based on random Fourier modes.

The free-stream turbulence level downstream of the turbulence generation zone is probed. The turbulence length scale is set to 1 mm

to accommodate the ability of the grid to resolve the turbulent eddies. In the experiment, $u' = 0.6\%$ and $v' = 0.4\%$ as measured by Giepman [10] at a lower Mach number of 1.7. It can be assumed that the higher Mach number of 2.3 means an even lower turbulence level for the current experiment. In the numerical simulation, the turbulence length scale is likely larger than the experiment due to the grid size limitation; therefore one might also expect that a lower turbulence intensity is required to achieve the same destabilization of the laminar shear layer.

The simulation is run with different turbulence levels (TI = 0.07%, 0.11%, and 0.21%) to investigate whether the free-stream turbulence has an effect on the shock oscillation. The spectral distribution of the imposed turbulence is shown in Fig. 29. The free-stream velocity is approximately 550 m/s. When the simulation is run with TI = 0.21% (Fig. 29a), the separated shear layer is fairly stable, and no significant laminar part of the separation bubble forms. The shock oscillation can therefore be said to be suppressed at TI = 0.21%. On the other hand, when TI = 0.11% (Fig. 29b), the shock oscillation does exist, and the amplitude is less than in the quiet inflow case, but the dynamic behavior and length of the laminar part of the shear layer more closely represent the experiment as opposed to a clean inflow simulation, due to the fact that the laminar separation shock travel distance in the clean inflow LES case is over 25 mm (150δ). After the initial tests, we decided to run the simulation at TI = 0.11% and TI = 0.07% (Fig. 29c), and the results are compared with the experiment. Volumetric numerical shadowgraphs are generated in situ (due to the high cost of saving the flow volume); for a comparison to the experimental shadowgraphs, keeping in mind that even though the numerical shadowgraphs are volumetric, they do not include the 3D end wall effects of the experiment. Three important phases of the shock oscillation mechanism are shown with the numerical shadowgraphs in Figs. 30a–30c. These numerical shadowgraph sequences are used in the same DMD

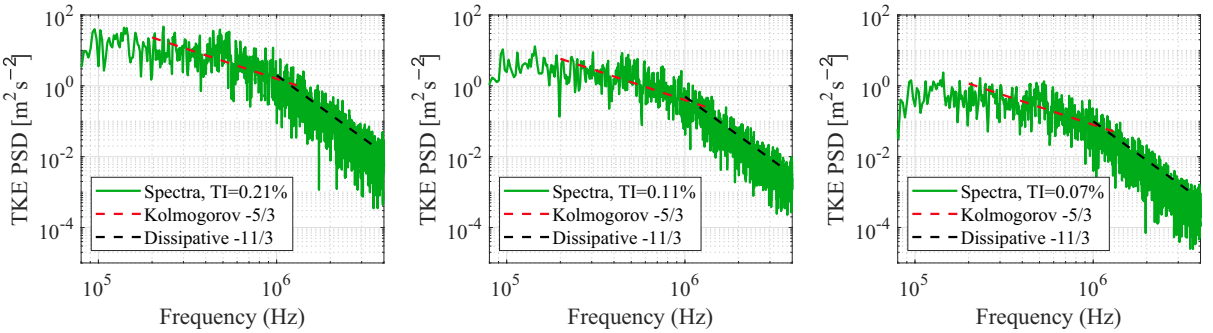

a) TI = 0.21% case **b) TI = 0.11% case** **c) TI = 0.07% case**

Fig. 29 Imposed turbulence turbulent kinetic energy spectra.

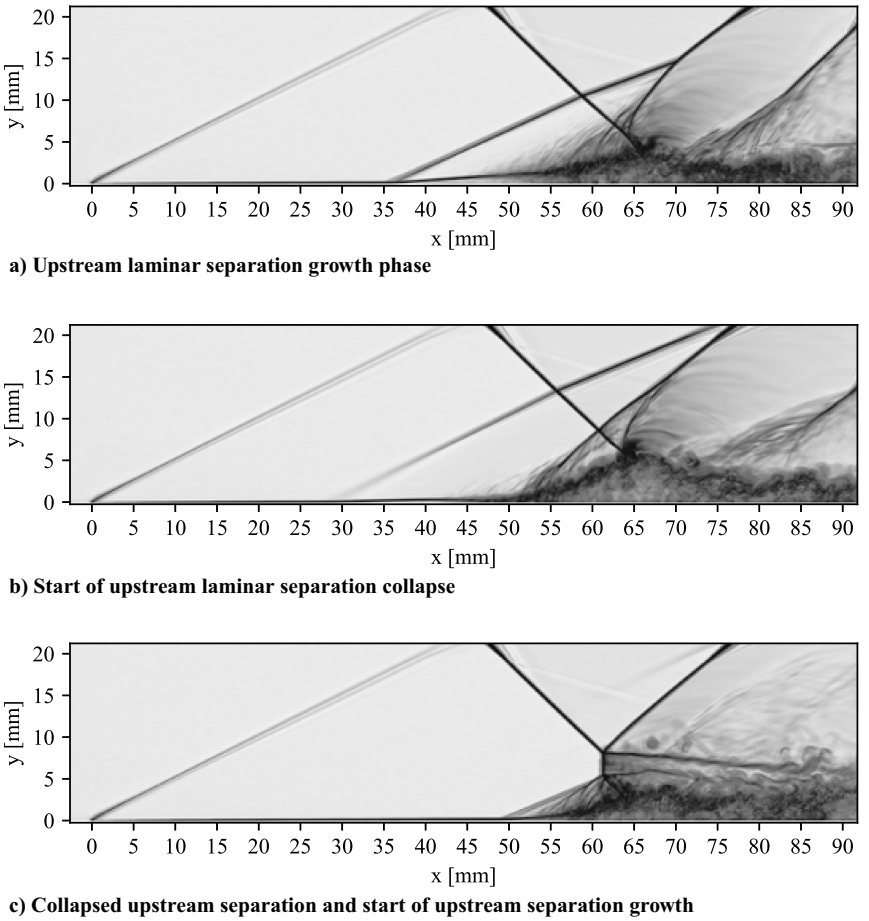

a) Upstream laminar separation growth phase

b) Start of upstream laminar separation collapse

c) Collapsed upstream separation and start of upstream separation growth

Fig. 30 Instantaneous numerical volumetric shadowgraphs of the LES simulation with TI = 0.07% depicting various phases of the shock oscillation.

algorithm to identify the dominant modes of shock oscillation. In Fig. 30a, the laminar separation is still growing in the upstream direction, with the shear layer at a steep angle. In Fig. 30b, the laminar part of the separation bubble started to collapse. The laminar separation shock starts to vanish at the upstream edge. Figure 30c shows the state after the collapse, with a new laminar separation shock starting to form. Note the size of the separation bubble is significantly reduced after the upstream instabilities from the collapse have advected over the bulk separation bubble (Fig. 30b vs Fig. 30c).

The shock oscillation mechanism originates in the upstream laminar section of the separation bubble. Therefore, we now zoom in on this part of the flow field in Fig. 31. This elongated and narrow part of the bubble propagates upstream, carrying turbulence originating from Kelvin–Helmholtz instabilities with it on the shear layer. When this section reaches a critical length, the instabilities become turbulent too far upstream, severing the laminar portion of the separation bubble. This leads to the collapse of the laminar part of the separation bubble and a suppression of the separation bubble as a whole, as the generated entrainment eddies are carried downstream over the bulk separation bubble. In Fig. 31: snapshot (1), the laminar part is suppressed, and about start to recover (2). From snapshots (2) to (7), we see the upstream propagation of the laminar separation shock emanating from the laminar part of the separation bubble. In snapshots (8) to (11), we see the collapse of the laminar part of the separation bubble. Note the vertical downward movement of the instabilities as they cut of the separation bubble region. Snapshots (11) and (12) show the coalescence of the compression wave region into a single shock wave when it retracts to the turbulent base of the separation bubble. In snapshot (14), the oscillation cycle starts to repeat, with a new laminar separation shock forming.

Because of the fact that the growth phase of the laminar part of the separation bubble dominates the shock oscillation, with the growth velocity matching between the experiment and the numerical simulations, as well as between different cases showing this oscillation mechanism [1], the characteristic length scale for the shock oscillation mechanism should be based on the distance of the laminar separation shock travel. To consistently identify this characteristic length of laminar separation shock travel for the Strouhal frequency, the standard deviations of spark-light shadowgraphs from the experiment are used in order to compare to those of the numerical shadowgraphs. Note that the experimental shadowgraphs in this upstream region would have less visual interference from end wall effects, because the separation bubble bulges forward at mid span as seen in the oil-flow visualization, which is advantageous for this purpose, and thus a good comparison with the numerical shadowgraphs can be achieved. The laminar separation shock travel distance in the experimental case can be seen in Fig. 32. This can be compared to the numerical cases for the two different turbulence levels in Figs. 33 and 34.

Note the difference in the indicated laminar separation shock travel distance when changing the free-stream turbulence level. Because the laminar separation shock travel velocity stays equal between the two cases, the frequency of oscillation changes. For the case with TI = 0.11%, the dominant oscillation frequency is 2672 Hz, whereas it is 2430 Hz for the TI = 0.07% case. We therefore conclude that the free-stream turbulence has a significant effect on the formation of the shear layer instabilities on the upstream growing laminar separation, and hence the free-stream turbulence affects the shock oscillation frequency.

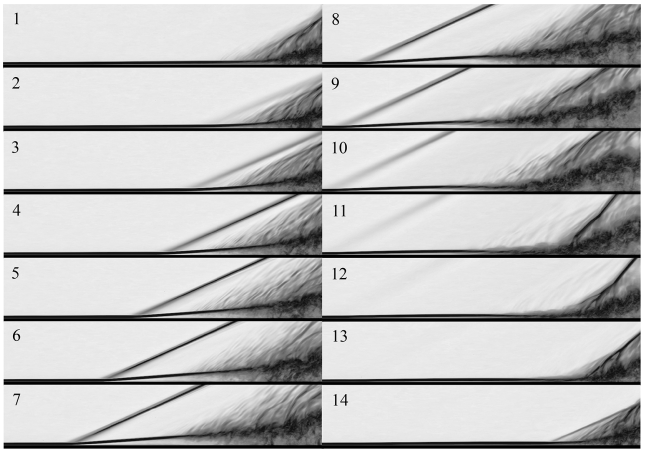

Fig. 31 Upstream view capturing growing and shrinking upstream part of separation bubble (Δt = 3.45e-05s). Numerical volumetric shadowgraph of the LES simulation with TI = 0.07%.

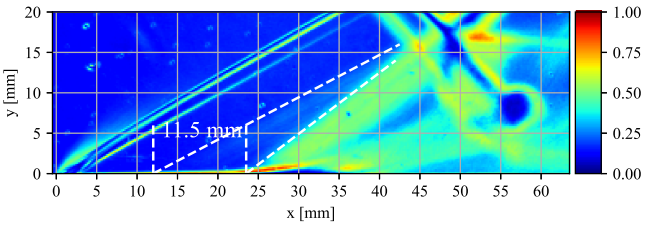

Fig. 32 Spark-light shadowgraph standard deviation.

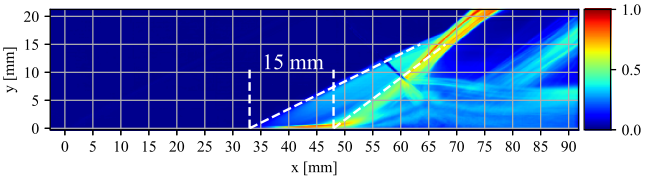

Fig. 33 Standard deviation of numerical volumetric shadowgraph of the LES simulation with TI = 0.11%.

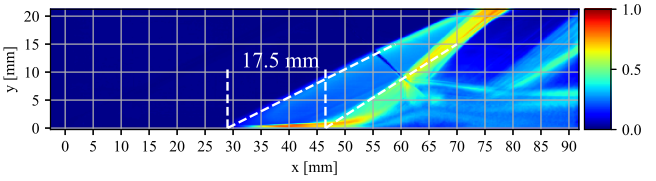

Fig. 34 Standard deviation of numerical volumetric shadowgraph of the LES simulation with TI = 0.07%.

Table 1 Strouhal frequencies for experiment and numerical simulations

	Experiment	Numerical TI = 0.07	Numerical TI = 0.11
L, mm	11.5	17.5	15
f, Hz	3728	2430	2672
St, -	0.078	0.077	0.073

Using the length scales calculated from the difference in abscissae of the emanating laminar and turbulent separation shocks in Figs. 32–34, we can nondimensionalize the dominant oscillation frequencies as listed in Table 1. The uncertainty of the Strouhal number attributed to fitted lines on the downstream turbulent separation shock and upstream laminar separation shock signatures of the standard deviation is estimated to be the order of 5% due to placement sensitivity to the x axis. The Strouhal frequencies are matching (around 0.075), with the difference in absolute frequency likely attributed to the fact that in the numerical simulation, the separation bubble collapse is more severe than in the experiment, due to the 3D effects in the experiment, with the end wall separation likely filling up the separation bubble earlier after the suppression, than in the numerical simulations which lack this aspect. Another reason for the difference might be that a turbulence level between 0.11% and 0.21% is needed for the numerical simulation in order to get a closer match of absolute frequencies.

VI. Conclusion

The investigation into the dynamics of highly separated transitional SBLIs aims to understand the mechanisms of shock oscillation and the how the state of the boundary layer influences this mechanism. This study contributes to understanding the mitigation of shock-induced

unsteadiness in transonic fans at altitude, where such interactions can lead to structural excitation and hence fan blade fatigue. The primary objective is to study the oscillation mechanisms from the laminar boundary-layer case, showing that the mechanism is eliminated in the turbulent (tripped boundary-layer) case, and to validate the oscillation mechanism observed in LES which are to be used by industry to resolve these phenomena.

The study employs high-speed Schlieren imaging, spark-light shadowgraphy, and surface oil-flow visualization to capture the dynamic behavior, instantaneous effects, and flow topology of the SBLI. The experiments were conducted using a 19 deg shock generator in a supersonic wind tunnel with a Mach number of 2.3 and a total pressure of 2.8 bar. High-speed Schlieren imaging at 100 kHz was used to observe the unsteady separation bubble, reflected shock movement, and periodically visible upstream laminar separation shock due to a periodically vanishing laminar part of the separation bubble. Spark-light shadowgraphy with 20 ns light bursts provided insights to the transition location and flow instabilities. Surface oil-flow visualization was employed to gauge the three-dimensional nature of the separation bubble. These experimental techniques were complemented by LES simulations, which captured the oscillation mechanisms in more detail.

For the laminar oncoming boundary layer, the oscillation mechanism is characterized by a periodically collapsing laminar section of the separation bubble, driven by instabilities on the laminar separated shear layer upstream of the shock: the periodic upstream movement of the thin and long laminar section of the separation bubble carries Kelvin–Helmholtz instabilities on its shear layer in the upstream direction, and, when a critical length is reached, the turbulence generated by the instabilities suppresses the upstream laminar section of the separation bubble, causing a collapse of this section. Furthermore, due to entrainment by the temporarily higher turbulence advecting downstream on the separation bubble shear layer, the entire separation bubble is temporarily partly suppressed, causing an oscillation of the reflected shock. The characteristic length scale for the oscillation mechanism, proposed based on the distance of the laminar separation shock's maximum upstream position relative to the turbulent separation shock, is a key finding. The Strouhal number, calculated to be approximately 0.075, aligns well with the LES results, validating the numerical approach to resolving the oscillation mechanism.

The turbulent boundary layer exhibits a different oscillation mechanism, with dominant frequencies significantly lower than those of the laminar case. The reflected shock movement in the turbulent SBLI is more rigid and less correlated with the separation bubble movement than the laminar case. This is evident from the significantly reduced reflected shock travel distance and different mode shapes, which show less correlation with the separation bubble dynamics and stiff shock movement, unlike the laminar case. The tripping of the boundary layer, achieved by a transition strip, effectively stabilizes the shock, as indicated by the significantly reduced reflected shock travel distance in the turbulent case compared to the laminar case.

The LES simulations captured these oscillation mechanisms in more detail and validated the experimental observations with regard to the shock oscillation mechanism. Additionally, LES results indicated that the shock oscillation mechanism is highly sensitive to free-stream turbulence levels, likely due to an earlier destabilization of the laminar shear layer for higher turbulence levels. With higher free-stream turbulence, the oscillation frequency increases due to the fact that the length of the laminar separation shock travel decreases, demonstrating a clear dependency on the upstream flow conditions.

In future work, the authors aim to capture the shock oscillation mechanism with particle image velocimetry for obtaining quantitative data at mid span, allowing a quantitative analysis of the separation bubble size, Mach stem size variation, and upstream separation bubble effects. Because corner effects obscure the true flow topology when using Schlieren techniques used in the current study, PIV will also provide a clear interpretation of the bulk separation bubble region flow features visible on the Schlieren.

It is further recommended that future numerical studies undertake full-span LES simulations of the fan at altitude, given that the shock oscillation mechanisms observed in LES were validated to be physically accurate, allowing studies on more complex industrial cases.

Appendix: Supplementary Graphs and Information

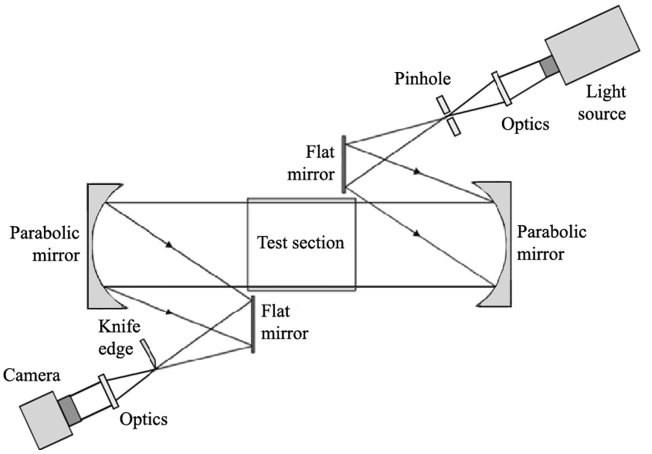

Fig. A1 Diagram showing Z-type Schlieren setup.

Table A1 Initial test matrix to find suitable experimental setup and boundary conditions

θ_{SG}	Ma	P_T [bar]	Observation	Remark
22 deg	2.3	4.0	Not started	Close (initial) mounting config.
19 deg	2.0	2.8	Not started	
19 deg	1.8	3.0	Not started	
19 deg	2.3	2.3	Not started	
19 deg	2.3	2.5	Less periodic oscillation	
19 deg	2.8	3.0	Low oscillation amplitude, less separation	
19 deg	2.3	2.8	Periodic oscillation	Chosen condition: low Re favorable
19 deg	2.3	3.0	Periodic oscillation	
19 deg	2.3	4.0	Less periodic oscillation	

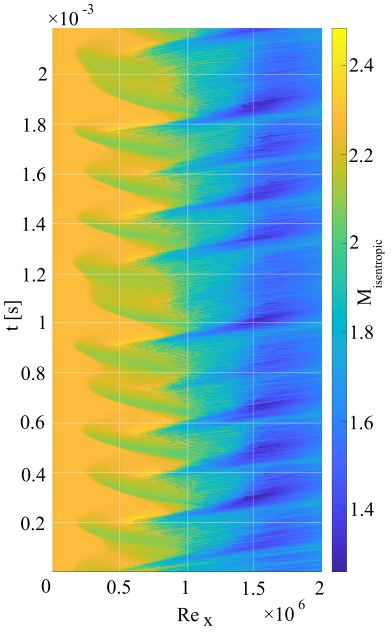

Fig. A2 Full DNS-resolution solution: isentropic Mach number distribution with time. Reproduced with permission from Nel et al. [1].

Acknowledgments

The author participated in the TEAMAero project, which has received funding from the European Union's Horizon 2020 research and innovation programme under grant agreement No 860909.

References

[1] Nel, P. L., Schreyer, A.-M., Schrijer, F., van Oudheusden, B., and Swoboda, M., "Research Configuration to Study Shock Oscillation Mechanism in Highly Loaded Transonic Fans," manuscript submitted for publication.

[2] Piponniau, S., Dussauge, J., Debieve, J. F., and Dupont, P., "A Simple Model for Low-Frequency Unsteadiness in Shock-Induced Separation," *Journal of Fluid Mechanics*, Vol. 629, June 2009, pp. 87–108. https://doi.org/10.1017/s0022112009006417

[3] Humble, R., Elsinga, G. E., Scarano, F., and van Oudheusden, B., "Three-Dimensional Instantaneous Structure of a Shock Wave/Turbulent Boundary Layer Interaction," *Journal of Fluid Mechanics*, Vol. 622, March 2009, pp. 33–62. https://doi.org/10.1017/s0022112008005090

[4] Nel, P. L., Janke, C., Vasilopoulos, I., Swoboda, M., Schreyer, A.-M., Hady, A., and Flaszynski, P., "Effect of Transition on Self-Sustained Shock Oscillations in Highly Loaded Transonic Rotors," *AIAA Journal*, Vol. 62, No. 6, 2024, pp. 2063–2075. https://doi.org/10.2514/1.J063378

[5] Ganapathisubramani, B., Clemens, N. T., and Dolling, D. S., "Large-Scale Motions in a Supersonic Turbulent Boundary Layer," *Journal of Fluid Mechanics*, Vol. 585, May 2006, pp. 369–394.

[6] Wu, M., and Martin, M., "Analysis of Shock Motion in Shock Wave and Turbulent Boundary Layer Interaction Using Direct Numerical Simulation Data," *Journal of Fluid Mechanics*, Vol. 594, Dec. 2007, pp. 71–83.

[7] Dupont, P., Haddad, C., and Debieve, J. F., "Space and Time Organization in a Shock-Induced Boundary Layer," *Journal of Fluid Mechanics*, Vol. 559, July 2006, pp. 255–277. https://doi.org/10.1017/S0022112006000124

[8] Diop, M., Piponniau, S., and Dupont, P., "High Resolution LDA Measurements in Transitional Oblique Shock Wave Boundary Layer Interaction," *Experiments in Fluids*, Vol. 60, March 2019, pp. 1–15. https://doi.org/10.1007/s00348-019-2701-x

[9] Robinet, J., "Bifurcations in Shock-Wave/Laminar-Boundary-Layer Interaction: Global Instability Approach," *Journal of Fluid Mechanics*, Vol. 579, May 2007, pp. 85–112. https://doi.org/10.1017/s0022112007005095

[10] Giepman, R., "Flow Control for Oblique Shock Wave Reflections," Ph.D. Dissertation, Technical Univ. of Delft, Delft, The Netherlands, 2016.

[11] Sartor, F., Mettot, C., Sipp, D., and Bur, R., "Dynamics of a Shock-Induced Separation in a Transonic Flow: A Linearized Approach," *43rd Fluid Dynamics Conference*, AIAA Paper 2013-2735, 2013. https://doi.org/10.2514/6.2013-2735

[12] Beresh, S. J., Clemens, N. T., and Dolling, D. S., "Relationship Between Upstream Turbulent Boundary Layer Velocity Fluctuations and Separation Shock Unsteadiness," *AIAA Journal*, Vol. 40, No. 12, 2002, pp. 2412–2422.

[13] Touber, E., and Sandham, N. D., "Oblique Shock Impinging on a Turbulent Boundary Layer: Low-Frequency Mechanisms," *38th AIAA Fluid Dynamics Conference*, AIAA Paper 2008-4170, 2008.

[14] Babinsky, H., and Harvey, J. K., *Shock Wave. Boundary-Layer Interactions*, Cambridge Univ. Press, Cambridge, England, U.K., 2011.

[15] Hergt, A., Grothe, P., Flaszynski, P., Szwaba, R., Piotrowicz, M., Kaczynski, P., Tartinville, B., and Hirsch, C., "Transition Location Effect on Shock Wave Boundary Layer Interaction, wp 3 Internal Flow Compressors," Notes on Numerical Fluid Mechanics and Multidisciplinary Designbook Series (NNFM), Vol. 144, Springer Nature, July 2020, pp. 229–296 [Online], https://elib.dlr.de/137310/.

[16] Cengel, Y., and Cimbala, J., *Fluid Mechanics Fundamentals and Applications*, 3rd ed., MCGRAW-HILL, US HIGHER ED, 2013.

[17] Nel, P. L., Schreyer, A.-M., Schrijer, F., van Oudheusden, B., and Swoboda, M., "Highly Separated Transitional Shockwave/Boundary-Layer Interactions: A Spatial Modal Study," *Physics of Fluids*, Vol. 36, No. 11, Nov. 2024, Paper 116114. https://doi.org/10.1063/5.0239390

[18] Weiner, A., and Semaan, R., "A Robust Dynamic Mode Decomposition Methodology for an Airfoil Undergoing Transonic Shock Buffet," *AIAA Journal*, Vol. 61, No. 10, 2023, pp. 4456–4467. https://doi.org/10.2514/1.J062546

[19] Weiner, A., and Semaan, R., "Backpropagation and Gradient Descent for an Optimized Dynamic Mode Decomposition," 2023, arXiv:2312.12928 [physics.flu-dyn].

[20] Schmid, P., and Sesterhenn, J., "Dynamic Mode Decomposition of Numerical and Experimental Data," *Journal of Fluid Mechanics*, Vol. 656, Nov. 2008. https://doi.org/10.1017/S0022112010001217

[21] Gavish, M., and Donoho, D. L., "The Optimal Hard Threshold for Singular Values is $4/\sqrt{3}$," *IEEE Transactions on Information Theory*, Vol. 60, No. 8, 2014, pp. 5040–5053. https://doi.org/10.1109/TIT.2014.2323359

[22] Nel, P. L., Grothe, P., Swoboda, M., Pirozzoli, S., and Weiss, J., "Towards Understanding and Resolving Natural Shock Oscillation in Transonic Compressors," *Advanced Computational Methods and Design for Greener Aviation*, edited by T. Tuovinen, J. Periaux, D. Knoerzer, G. Bugeda, and J. Pons-Prats, Springer, Cham, 2024, pp. 75–93. https://doi.org/10.1007/978-3-031-61109-4_6

[23] Nicoud, F., Benoit, J., Marsden, O., and Vervisch, L., "Using Singular Values to Build a Subgrid-Scale Model for Large Eddy Simulations," *Physics of Fluids*, Vol. 23, No. 8, 2011, pp. 85–106.

[24] Davidson, L., "Using Isotropic Synthetic Fluctuations as Inlet Boundary Conditions for Unsteady Simulations," *Advances and Applications in Fluid Mechanics*, Vol. 1, 2007, pp. 1–35 [Online], https://api.semanticscholar.org/CorpusID:73545406.

M. M. Choudhari
Associate Editor